Biomech Model Mechanobiol (2013) 12:335–348
DOI 10.1007/s10237-012-0402-y

ORIGINAL PAPER

Vortical flow in the utricle and the ampulla: a computational study on the fluid dynamics of the vestibular system

Francesco Boselli · Dominik Obrist · Leonhard Kleiser

Received: 10 October 2011 / Accepted: 28 April 2012 / Published online: 16 May 2012

Abstract We present a computational study of the fluid dynamics in healthy semicircular canals (SCCs) and the utricle. The SCCs are the primary sensors for angular velocity and are located in the vestibular part of the inner ear. The SCCs are connected to the utricle that hosts the utricular macula, a sensor for linear acceleration. The transduction of angular motion is triggered by the motion of a fluid called endolymph and by the interaction of this fluid with the sensory structures of the SCC. In our computations, we observe a vortical flow in the utricle and in the ampulla (the enlarged terminal part of the SCCs) which can lead to flow velocities in the utricle that are even higher than those in the SCCs. This is a fundamentally new result which is in contrast to the common belief that the fluid velocities in the utricle are negligible from a physiological point of view. Moreover, we show that the wall shear stresses in the utricle and the ampulla are maximized at the positions of the sensory epithelia. Possible physiological and clinical implications are discussed.

Keywords Vestibular system · Endolymph flow · Semicircular canals (SCC) · Utricular macula · Mechanotransduction

1 Introduction

The inner ear is carved into the temporal bone (bony labyrinth) and hosts the structures responsible for the sense of hearing (cochlea) and for the sense of balance (vestibular system). The human vestibular system (Fig. 1) consists, bilaterally, of three sensors for angular velocity—the horizontal (HC), the anterior (AC), and the posterior (PC) semicircular canals (SCCs)—and two sensors for gravity and linear acceleration—the utricular and the saccular otolith organs. These biological sensors belong to a membranous duct (the membranous labyrinth), which occupies part of the lumen of the bony labyrinth (Curthoys et al. 1977) to which it is rigidly fixed. The gap between the membranous wall and the bone is filled with perilymph, while the membranous lumen is filled with endolymph. Both fluids have mechanical properties similar to water (Steer et al. 1967). The SCCs are three slender ducts spanning an angle of approximately 250° and merging into a bigger chamber, the utricle, which hosts the utricular otolith organ. All SCCs are plugged at one end by a supple gelatinous structure called cupula. The section where the cupula is situated has a larger cross-section than the rest of the slender SCC and is called ampulla. A sensory structure, the crista ampullaris, protrudes from the wall of the ampulla. It is embedded into the base of the cupula and is populated by innervated hair cells. During head rotations, the inertia of the endolymph leads to a deflection of the cupula and the embedded hair cell bundles. This is the origin of the afferent signals leading to the sensation of angular motion.

The sensory epithelium in the utricle, the utricular macula, occupies part of the utricular wall. It is a layered membrane topped with dense calcium crystals, called otoconia, leaning toward the endolymph space (Kachar et al. 1990). The otoconia are denser than the surrounding endolymph such that linear accelerations can lead to relative movements of the dense otoconia layer with respect to the skull. This deflects the hair cell bundles embedded in the underlying elastic layers and triggers the neurological signal.

A more detailed introduction to the physiology and the biomechanics of the vestibular system can be found in Grant (1995) and Rabbitt et al. (2004). A recent review is given by Kondrachuk et al. (2011).

F. Boselli (✉) · D. Obrist · L. Kleiser
Institute of Fluid Dynamics, ETH Zurich, Sonneggstrasse 3, 8092 Zurich, Switzerland
e-mail: boselli@ifd.mavt.ethz.ch

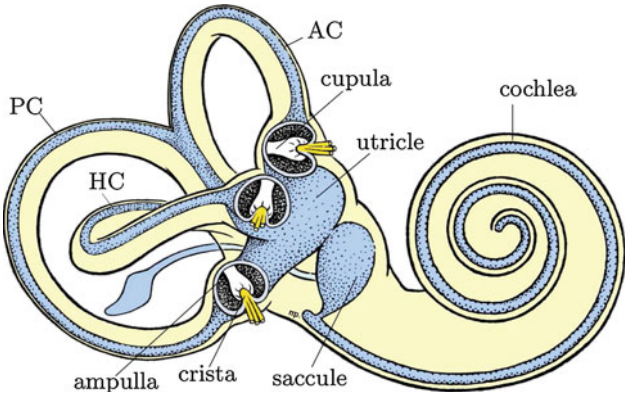

Fig. 1 The membranous labyrinth (*blue*) and the bony labyrinth (*yellow*) of the inner ear (adapted from Obrist et al. 2010, with permission from Elsevier). The width of the membranous anterior (AC), posterior (PC), and horizontal (HC) canals is exaggerated for better visibility. In reality their diameter is only about 5 % of the diameter of the bony canals (Curthoys et al. 1977)

1.1 Biomechanics of the SCCs

The gross behavior of a SCC can be modeled mathematically as a band-pass filter, which is defined by the transfer function

$$\hat{V}/\hat{\dot{\alpha}} \approx -\frac{i\omega G}{(i\omega + \tau_c^{-1})(i\omega + \tau_s^{-1})} \tag{1}$$

with a constant G, a lower cut-off frequency τ_c^{-1} and an upper cut-off frequency τ_s^{-1}. For head movements within this frequency (ω) range, the cupula displacement V (to be defined later) is proportional and in phase with the angular velocity $\dot{\alpha}$ of the head in the plane of the SCC ($\hat{V}$ and $\hat{\dot{\alpha}}$ indicate the respective Laplace-transformed variables). Several models of increasing complexity have been proposed to relate the values of τ_c, τ_s, and G to the actual anatomy and physics of the SCCs (Van Buskirk et al. 1976; Pardoe and Haughton 1979; Bernard 1982; Oman et al. 1987; Rabbitt and Damiano 1992; Damiano and Rabbitt 1996; Ifediba et al. 2007; Obrist 2008; Vega et al. 2008). All these models lead qualitatively to similar results. It turns out that the "long" time constant τ_c is related to the stiffness K of the cupula. In contrast, the "short" time constant τ_s is mainly related to the lumen of the slender duct and the viscosity of the endolymph. The volumetric gain $|\hat{V}/\hat{\dot{\alpha}}|$ increases with the cross-sectional area and the major radius of the slender duct.

What we have discussed so far is usually referred to as the macro-mechanics of the SCCs (Rabbitt et al. 2004) and is limited to describing the endolymph flow in terms of bulk flow rates. Such mean values are obtained by assuming a Poiseuille-like flow *a priori*. A more detailed analysis has been carried out by Damiano and Rabbitt (1996), where the deflected shape of the cupula has been obtained under the assumption of an axisymmetric flow profile. In the utricle, the flow velocities are usually assumed to be significantly smaller than in the SCCs such that they do not contribute significantly to the physiology of the SCCs (Van Buskirk 1977) and the utricular otolith.

In the present work, we employ a numerical model for studying the three-dimensional fluid dynamics in the SCCs and the utricle in detail, and we will present flow patterns in the ampulla and the utricle, which were not shown so far. They lead to significantly higher flow velocities in the proximity of the sensory epithelia than a Poiseuille-like flow. This is relevant for the mechanotransduction. The relationship between these flow patterns and the macroscopic features of the anatomy is also studied.

2 Methods

The elasticity of the membranous duct is believed to play a minor role during physiological head maneuvers (Yamauchi et al. 2002). Therefore, the perilymph is neglected in our simulations and the membranous labyrinth is modeled as a rigid structure fixed to the skull and filled with endolymph. The endolymph is treated as an incompressible Newtonian fluid with mechanical properties similar to water (density $\rho = 1{,}000\ \mathrm{kg/m^3}$; viscosity $\mu = 0.001$ Pa s). Here, we only consider angular accelerations in the plane of a single canal. The geometry of the labyrinth is simplified to a single SCC connected with the utricle.

2.1 Governing equations

We observe the endolymph flow from a reference frame rotating with the membranous labyrinth, that is, fixed to the skull. We model this flow as a creeping flow, because the estimated Reynolds number (Re) is small,

$$\mathrm{Re} = \rho \bar{U} a_c/\mu \approx O(10^{-3})$$

where $\bar{U} \approx O(10^{-5}\ \mathrm{m/s})$ is a typical velocity in the SCC (e.g. Obrist 2008), and $a_c \approx O(10^{-4}\ \mathrm{m})$ is the typical radius of the canal lumen. We limit our simulations to head maneuvers at low to moderate frequencies ($\lesssim$1 Hz) such that we can neglect the short time constant τ_s and the fast duct modes described by Obrist (2008). Under these assumptions, the governing equations for the endolymph flow are the Stokes equations,

$$-\nabla p(\mathbf{x}) + \mu \nabla^2 \mathbf{u}(\mathbf{x}) = \mathbf{f}(\mathbf{x}, t) \tag{2a}$$

$$\nabla \cdot \mathbf{u}(\mathbf{x}) = 0 \tag{2b}$$

with no-slip boundary conditions at the wall; t is the time, $\mathbf{x} = (x_1, x_2, x_3)$ are the coordinates, and p and $\mathbf{u} = (u_1, u_2, u_3)$ are the pressure and the velocity of the fluid, respectively. The forcing term $\mathbf{f} = \mathbf{f}_\alpha + \mathbf{f}_c$ is a superposition of fictitious forces $\mathbf{f}_\alpha$ arising from the rotational acceleration and the force $\mathbf{f}_c$ of

the cupula acting on the fluid. Because Eq. (2) is linear, we can express $\mathbf{u}$ by the linear superposition

$$\mathbf{u} = \mathbf{u}_\alpha + \mathbf{u}_c \tag{3}$$

where $\mathbf{u}_\alpha$ and $\mathbf{u}_c$ are computed independently by setting $\mathbf{f} = \mathbf{f}_\alpha$ and $\mathbf{f} = \mathbf{f}_c$, respectively. Here, $\mathbf{u}_\alpha$ represents the flow which is induced by the rotation of the head in a canal with relaxed cupula (or no cupula) and $\mathbf{u}_c$ is the flow induced by the cupula.

The force $\mathbf{f}_c$ is modeled as in previous works (e.g. Van Buskirk et al. 1976; Oman et al. 1987) by introducing a time-dependent pressure difference ΔP across the cupula. This pressure is proportional to the volume V of fluid displaced during a head maneuver,

$$\Delta P(t) = -K V(t) \tag{4}$$

where K is the stiffness of the cupula. The volumetric displacement $V(t)$ of the cupula can be computed by integrating the flow rate at any cross-section A_c of the SCC with respect to time,

$$V(t) = \int_0^t \iint_{A_c} \mathbf{u} \cdot \mathbf{n}_c \, \mathrm{d}A \, \mathrm{d}t \tag{5}$$

where $\mathbf{n}_c$ is the normal vector on the surface A_c. Integral (5) is solved numerically by means of Gauss quadrature (Abramowitz and Stegun 1992) and explicit time integration. The volumetric displacement $V(t)$ describes the macro-mechanics of the cupula-endolymph system and dominates the dynamics of the SCC.

The pressure difference (4) leads to the flow $\mathbf{u}_c$, which turns out to be a Poiseuille-like flow proportional to the stiffness K and the volumetric cupula displacement $V(t)$. (See Appendix A for an explicit approximate formula for $\mathbf{u}_c$ in function of an axially variable lumen in the SCC).

The force $\mathbf{f}_\alpha$ is explicitly related to the angular acceleration $\ddot{\boldsymbol{\alpha}}$ (Appendix B),

$$\mathbf{f}_\alpha(\mathbf{x}, t) = \rho \ddot{\boldsymbol{\alpha}} \times \mathbf{x} \tag{6}$$

with the center of rotation at the origin. The velocity field $\mathbf{u}_\alpha$ is then computed numerically with the multilayer method of fundamental solutions (multilayer MFS, Appendix C).

The appropriateness of the employed Stokes equations was verified *a posteriori* by repeating some of the simulations by a finite volume code (OpenFOAM). It solves the full Navier-Stokes equations, including effects of unsteadiness and a rotating reference frame (B. Grieser, private communication).

As we will show in the following, the present method is an accurate description of the low-frequency cupula-endolymph dynamics in SCCs.

3 Results

3.1 Endolymph flow during a head maneuver in the plane of the horizontal canal

We apply our numerical model to a head movement, which rotates the head in the plane of the horizontal canal (HC) by 120° in 3 s. To obtain a smooth acceleration pattern $\ddot{\alpha}$, we use the function chosen by Obrist et al. (2010),

$$\alpha(t) = \begin{cases} 0, & t < 0\text{s} \\ \frac{2\pi}{3\times 2187}(2187 - 20t^7 - 210t^6 & \\ \qquad -756t^5 - 945t^4), & 0\text{ s} \leqslant t \leqslant 3\text{s} \\ \frac{2\pi}{3}, & t > 3\text{s}. \end{cases} \tag{7}$$

The resulting angular acceleration, angular velocity, and angular position α of the head during the head maneuver are shown in Fig. 2a.

For validation purposes, we show results that were obtained by idealizing the SCC to a torus of major radius 3 mm and circular cross-sections of constant radius 0.16 mm. The equation for the endolymph dynamics proposed by Van Buskirk et al. (1976) can be adapted to this specific case by setting the angle spanned by the utricle to zero and the angle spanned by the slender duct to 2π. The resulting equations were solved as described by Obrist (2008) to provide a reference solution. The cupula volume displacements obtained from our numerical solution and the reference solution are shown in Fig. 2b for $K = 13$ GPa/m^3. These results demonstrate the ability of our model to accurately predict the low-frequency dynamics of the SCCs.

Next, we consider the geometrical model of the right HC shown in Fig. 3. This geometry is symmetric with respect to the (x_1, x_2)-plane and its cross-sections are approximated by ellipses. The ellipticity of the cross-sections is defined as

$$e = a_2/a_1, \tag{8}$$

where a_1 and a_2 are the horizontal and vertical axes parallel and perpendicular to the canal plane, respectively. If $e > 1$ the major axis is the vertical axis. The cross-sectional area and ellipticity along the centerline (Fig. 4) are obtained by interpolating and smoothing the anatomical data reported in Figure 3 of Curthoys and Oman (1987). The actual relaxation time of the cupula (τ_c) is under debate and could vary significantly between patients. Therefore, the simulations were repeated for several values of K leading to values of τ_c from 4.2 to 104 s. These values are motivated by data reported in Grant and Van Buskirk (1976), Rabbitt et al. (2009), Selva et al. (2009). The resulting cupula volume displacements $V(t)$ are plotted in Fig. 2c. The macro-mechanics of our model is consistent with the results reported in the literature (e.g. Van Buskirk et al. 1976; Pardoe and Haughton 1979;

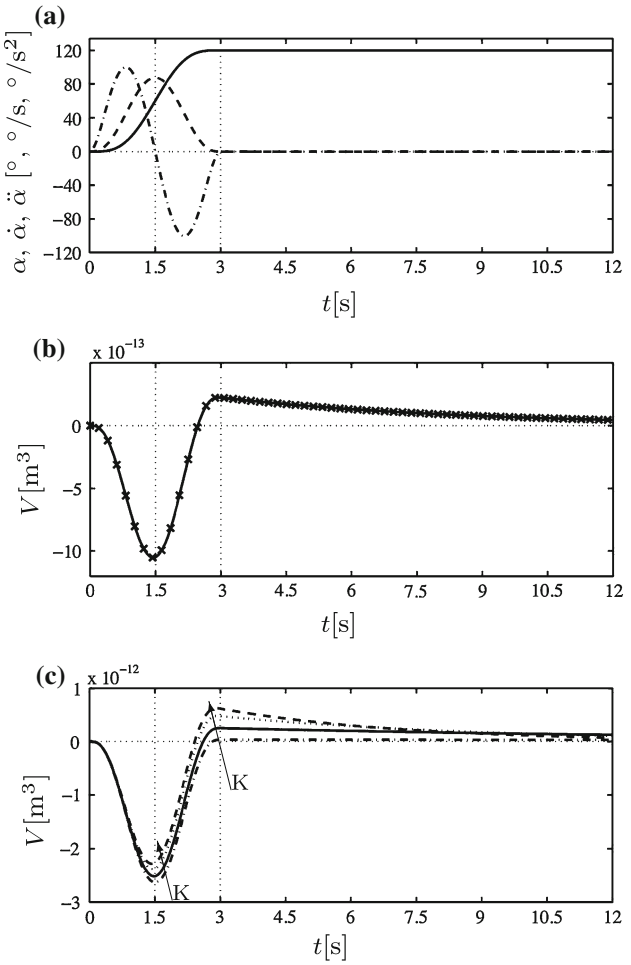

Fig. 2 (**a**) Head maneuver (*solid line* angular position α; *dashed line* angular velocity $\dot{\alpha}$; *dashed line with dot* angular acceleration $\ddot{\alpha}$). Resulting cupular volume displacement $V(t)$ against time (**b**) when the geometry of the SCC is idealized to a torus with constant circular cross-sections, major radius 3 mm and minor radius 0.16 mm (*solid line* numerical model; *multiplication symbol* reference data from Van Buskirk's model), and (**c**) for a realistic geometry (cf. Fig. 3) and different values of the cupula time constants τ_c(s) and the cupula stiffness K(GPa/m^3) (*dashed line* $\tau_c = 4.2$, $K = 7.14$; *dotted line* τ_c=6, $K = 5$; *solid line* $\tau_c = 13$, $K = 2.3$; *dashed line with dot* $\tau_c = 104$, $K = 0.288$)

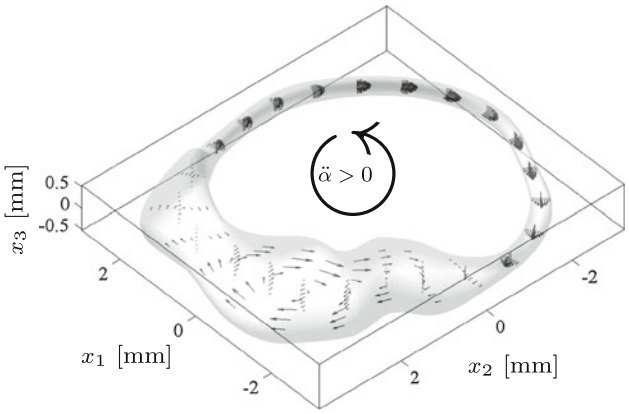

Fig. 3 Anatomical model of the HC with utricle (*shaded surface*) and instantaneous velocity vectors (*arrows*) sampled along the major and the minor axes of some cross-sections for a positive angular acceleration $\ddot{\alpha} > 0$ in the plane of the canal

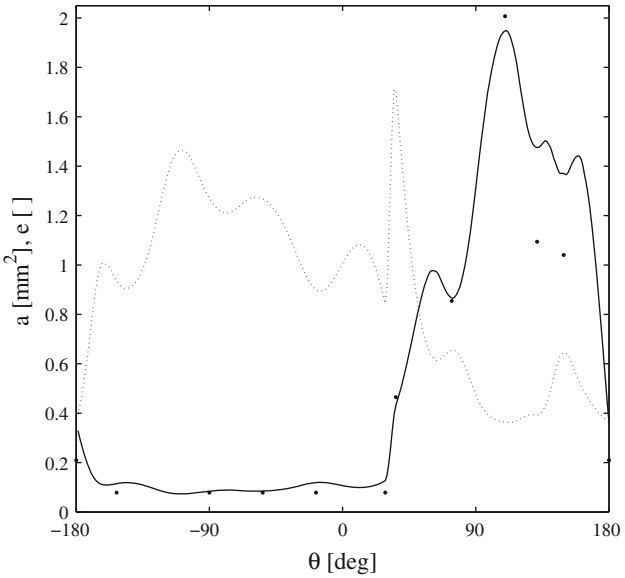

Fig. 4 Cross-sectional area a (*solid line*) and ellipticity e (*dotted line*) of the endolymphatic duct shown in Fig. 3 and cross-sectional area a (*bullets*) from Curthoys and Oman (1987). θ is the azimuthal coordinate of the duct centerline points

Bernard 1982; Oman et al. 1987; Rabbitt and Damiano 1992; Damiano and Rabbitt 1996; Ifediba et al. 2007; Obrist 2008; Vega et al. 2008). The volumetric displacement V is approximately proportional to the angular velocity $\dot{\alpha}$ of the head. The overshoot of the cupula at the end of the head maneuver [described mathematically in Obrist (2008)] reflects the mechanical adaptation of the cupula. Increasing the stiffness K reduces the maximum cupula displacement slightly (Fig. 2c, at $t \approx 1.5$ s) and increases the cupula overshoot at $t = 3$ s. Because the system is over-damped, the overshoot does not lead to oscillations of the cupula. Instead, it decays exponentially to zero with relaxation time τ_c (Fig. 2c, $t > 3$ s).

Furthermore, we observe a Poiseuille-like flow in the slender part of the SCC, which is consistent with the models available in the literature.

In the utricle and the ampulla (the enlarged regions of our model labyrinth), the cross-sectional areas are one order of magnitude larger than in the slender duct and the velocities do not exhibit a parabolic profile. Instead, we observe an S-shape velocity profile typical of a vortex (Fig. 5). With respect to a rotating reference frame fixed to the skull, this vortex rotates in the plane of the canal and leads to velocities in the utricle, which are of the same order of magnitude as the velocities in the slender duct, that is, $O(10^{-5}$ m/s) for $\ddot{\alpha} \approx 100°/s^2$. This is a fundamentally new result and contradicts previous

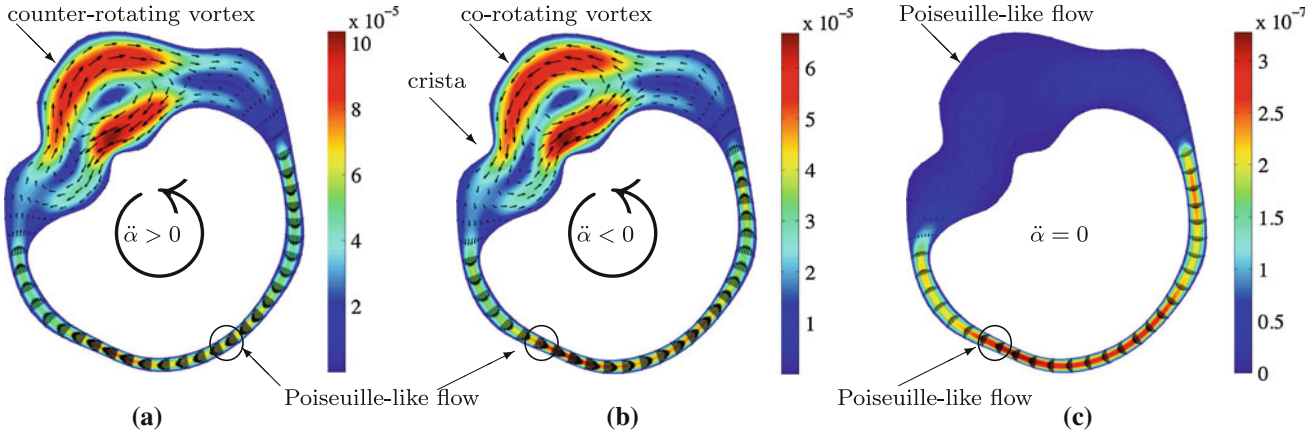

Fig. 5 Velocity field in plane $x_3 = 0$ at (**a**) $t = 0.8$ s (flow regime I; acceleration), (**b**) $t = 1.8$ s (flow regime II; deceleration), end (**c**) $t = 4$ s (flow regime III; zero acceleration) for the head maneuver given in Eq. (7) and plotted in Fig. 2a. The *arrows* indicate velocity vectors, while the *color* shows the velocity magnitude in m/s. ($\tau_c = 16$ s). The *big arrows* at the center indicate the direction of head rotation

models predicting axisymmetric flows and lower velocities in the enlarged regions of the labyrinth. The flow velocities in the utricle predicted on the basis of a Poiseuille-like flow would be approximately one order of magnitude smaller than the actual velocities we observe.

During and after the head maneuver, we can recognize three flow regimes: (I) a head-acceleration regime, (II) a head-deceleration regime, and (III) a post-maneuver regime (Fig. 5). During the head-acceleration regime I (0 s $< t <$ 1.5 s), the endolymph in the slender duct and the vortex in the enlarged regions flow opposite to the angular velocity of the head; during the head-deceleration regime II (1.5 s $< t <$ 3 s) the endolymph flow reverses direction such that the vortex co-rotates with the head. At the end of the head maneuver, the cupula volume displacement is non-zero because of the overshoot discussed earlier. The elastic cupula returns then slowly to its resting position, which induces a Poiseuille-like positional flow in the whole fluid domain (flow regime III). It turns out that the velocity $\mathbf{u}_\alpha$ induced by angular acceleration is responsible for the observed vortex. No vortex is observed during flow regime III because the positional flow is only due to the elastic force of the cupula and $\mathbf{u}_\alpha$ is zero as $\ddot{\alpha} = 0°/s^2$.

It is worthwhile noting that the direction of the flow velocities close to the crista are the same whether one considers a Poiseuille or an S-shape profile within the ampulla (Fig. 5). However, the S-shape profile enhances the deflection of the hair cell bundles embedded in the cupula, because the peak velocity is higher and closer to the crista than for a Poiseuille flow. Figure 6 shows that the displacement of a point on the cupula close to the crista can be one order of magnitude bigger for the S-profile.

We repeated the last simulation by modeling the cupula as a solid wall. We still observe vortical flows just next to the cupula, although the velocity at the cupula is obviously

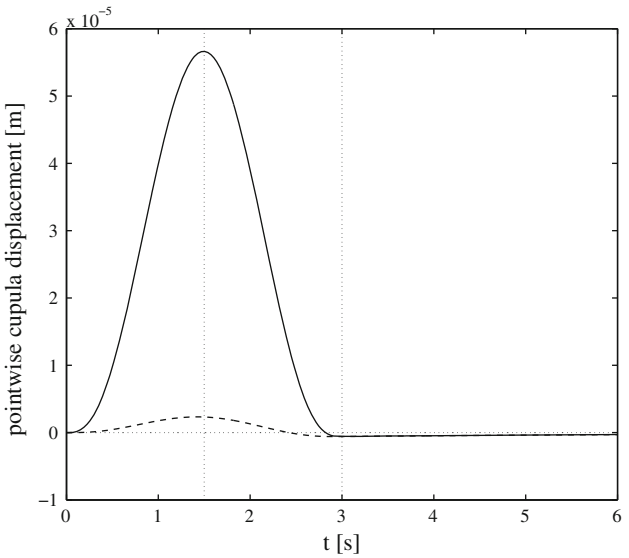

Fig. 6 Displacement of a point close to the crista (shown in Fig. 5) against time. Results for the computed vortical S-profile (*solid line*) and for a Poiseuille profile (*dashed line*) of equal flow rate ($\tau_c = 4.6$ s)

zero. This suggests that the presence of the observed vortex should be expected regardless of the cupula stiffness.

3.1.1 Shear stresses at the wall

The wall shear stresses caused by the viscous forces of the endolymph flow in the enlarged part of the labyrinth are of the same order of magnitude as in the slender canal. The maximum value predicted on the basis of a Poiseuille flow in the utricle would be an order of magnitude smaller.

A closer look at the shear stress distribution in the enlarged region of the labyrinth suggests that the ellipticity of the

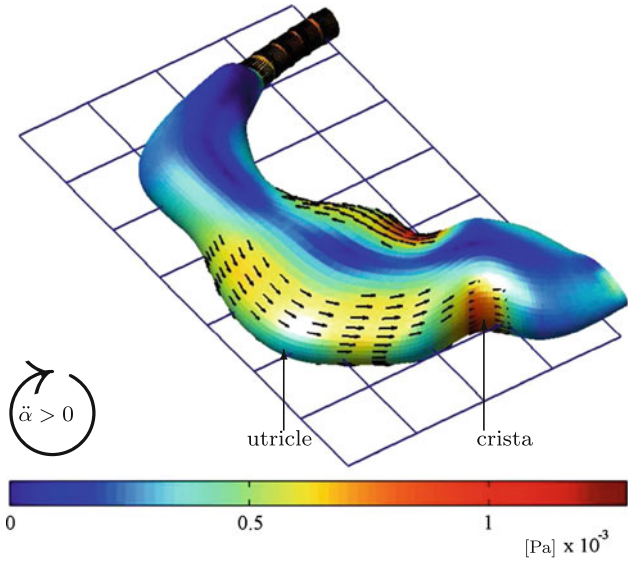

Fig. 7 Shear stresses at the wall of the utricle and the horizontal ampulla for a head acceleration in the plane of the HC. The values are shown for $\ddot{\alpha} = 120°/s^2$

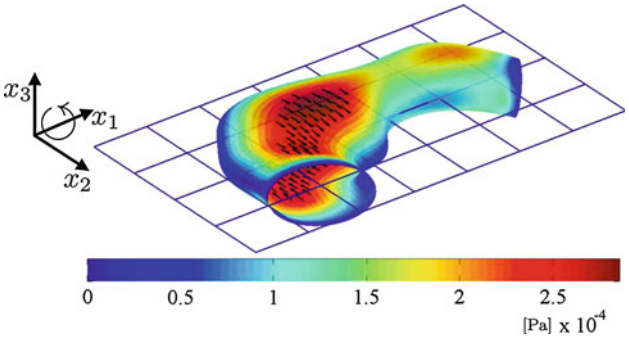

Fig. 8 Shear stresses at the wall of the utricle for an angular acceleration in the plane of the PC ($\ddot{\alpha} = 120°/s^2$)

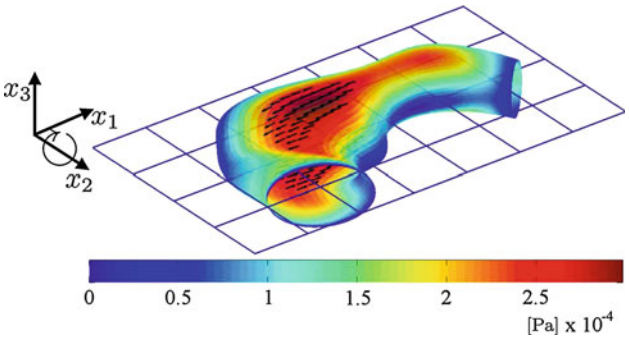

Fig. 9 Shear stresses at the wall of the utricle for an angular acceleration in the plane of the AC ($\ddot{\alpha} = 120°/s^2$)

cross-section plays a fundamental role in the shear stress distribution. During rotations in the plane of the HC, the ellipticity of the utricle is such that the peak values of the velocity profile are closer to the upper and lower parts of the utricular wall than to the outer and inner walls. As a consequence, we observe peak values of the wall shear stresses at the upper and lower parts of the utricular wall rather than at the outer and inner ones (Fig. 7). This result is remarkable, since the utricular macula is positioned at the lower part of the utricular wall. In the ampulla, the cross-sectional ellipticity is closer to one such that the maximum is at the outer wall of the ampulla where the crista is located.

If we compute the shear stresses in a plugged utricle (obtained by closing the connections of the utricle with the SCC), the results do not deviate significantly from the results in the utricle in Fig. 7. Such a configuration is mechanically equivalent to a rigid cupula and tells us that the stiffness of the cupula and the geometry of the slender SCCs do not influence significantly the flow in the utricle. Therefore, we can use this plugged utricle to estimate the wall shear stresses induced by head rotations in planes orthogonal to the plane of the HC (e.g., about the x_1 or x_2 axis).

The utricle in our geometry is oriented approximately along the x_1 axis and angular accelerations $\ddot{\boldsymbol{\alpha}} = (\ddot{\alpha}, 0, 0)$ and $\ddot{\boldsymbol{\alpha}} = (0, \ddot{\alpha}, 0)$ mimic head rotations in the planes of the PC and the AC, respectively. We observe a vortex in the respective plane of rotation also for these two accelerations. The resulting shear stresses are largest at the central region of the flat utricular walls (Figs. 8, 9), that is, close to the utricular macula. This suggests that the anatomy of the labyrinth is such that it maximizes the shear stresses induced by endolymph flow at the sensory epithelia for accelerations in any direction. The directions of the resulting shear stresses at the macula depend on the plane of rotation. They are mainly directed along the x_2 axis for rotations in the (x_2, x_3)-plane (Fig. 8) and along the x_1 axis for rotations in the (x_1, x_3)-plane (Fig. 9). For accelerations in the plane of the HC, the direction of the shear stresses follows the S-shape pattern of the vortex in the macula plane, such that different regions of the macula experience shear stresses along different directions (Fig. 7). Note that results for specific values of $\ddot{\alpha}$ can be obtained by linear rescaling of the results in Figs. 7, 8, and 9, which are given for a typical head acceleration of $\ddot{\alpha} = 120°/s^2$.

3.2 Influence of the morphology of the utricle on the endolymph flow velocities: a parametric study

In this section, we present results from a parametric study on the influence of the morphology of the labyrinth on the formation of the vortex. For this specific study, we neglect the cupula ($K = 0$) and idealize the vestibular labyrinth as a toroidal duct with constant radius of curvature $R_{scc} = 3$ mm. The cross-sectional area and ellipticity are parametrized as a function of the azimuthal coordinate θ. This idealized geometry consists of two regions. A slender duct of

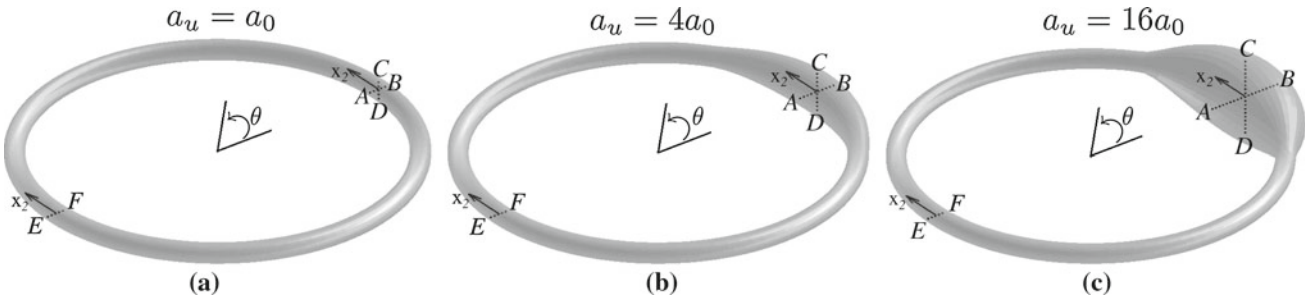

Fig. 10 Type I geometries (circular cross-sections) for different ratios of the utricular (a_u) and SCC (a_0) cross-sectional areas: (**a**) $a_u/a_0 = 1$, (**b**) $a_u/a_0 = 4$, and (**c**) $a_u/a_0 = 16$. $\overline{AB}$ and $\overline{CD}$ are the horizontal and vertical axes of the central utricular cross-section, respectively; $\overline{EF}$ is the diameter of the slender duct. $\overline{AB} = \overline{CD} = \overline{EF}\sqrt{a_u/a_0}$

constant cross-sectional area $a_0 = 0.16^2\pi$ mm^2 and ellipticity $e_0 = 1$ representing the slender part of the SCC, and a second region spanning an angle β with increased cross-sectional area and ellipticity $e_u(\theta)$ representing the utricular bulge ($-\beta/2 \le \theta \le \beta/2$). The cross-sectional area is parametrized as follows

$$a(\theta) = \begin{cases} a_0, & -\pi \le \theta < -\beta/2 \\ c_4\theta^4 + c_2\theta^2 + c_0 + a_0, & -\beta/2 \le \theta < \beta/2 \\ a_0, & \beta/2 \le \theta < \pi \end{cases} \quad (9)$$

where $c_0 = a_u - a_0$, $c_2 = -2c_0/(\beta/2)^2$, $c_4 = -c_2/2/(\beta/2)^2$ and a_u is the area of the biggest cross-section in the utricular region at $\theta = 0$.

We introduce three families of geometries that differ from each other only in the ellipticity of the utricular region e_u:

Type I: All the cross-sections are circles ($e_u = 1$ for all θ).

Type II: "Oblate utricle" ($e_u(\theta) = a_0/a(\theta) < 1$ for $-\beta/2 < \theta < \beta/2$). The vertical axes of the utricular cross-sections equal the radius r_0 of the slender duct ($r_0 = \sqrt{a_0/\pi}$). Increasing a_u leads to a "horizontal" expansion of the utricular bulge.

Type III: "Prolate utricle" ($e_u(\theta) = a(\theta)/a_0 > 1$ for $-\beta/2 < \theta < \beta/2$). The horizontal axes of the utricular cross-sections equal the radius r_0 of the slender duct. Increasing a_u leads to a "vertical" expansion of the utricular bulge (equivalent to Type II but with the utricular region rotated by 90°).

We first consider Type I geometries with $\beta = 0.42\pi$ (Fig. 10) and study how the flow profile in the utricular region changes as a function of the ratio a_u/a_0. When the SCC is approximated by a torus of constant cross-sectional area ($a_u/a_0 = 1$), the flow profile (yellow curve in Fig. 11) is identical at each cross-section and is well approximated by an axisymmetric parabolic flow. When we increase the utricular

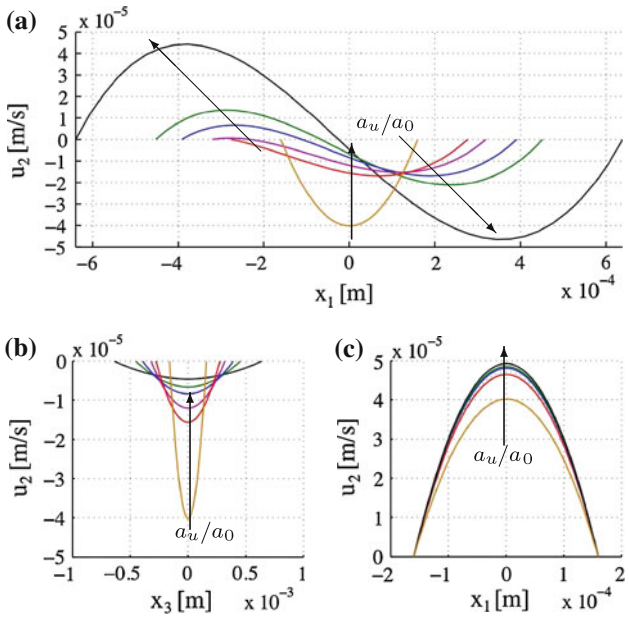

Fig. 11 Axial velocity u_2 evaluated for $\ddot{\alpha} = 120°/s^2$ along the (**a**) horizontal ($\overline{AB}$) and (**b**) vertical ($\overline{CD}$) axes of the cross-section at the center of the utricular region ($\theta = 0$) and (**c**) along the horizontal axis ($\overline{EF}$) of the opposite cross-section in the slender duct region (at $\theta = \pi$). The zeros of the abscissae correspond to the center of the cross-section. The results are obtained for different ratios of the utricular (a_u) and SCC (a_0) cross-sectional areas (*yellow* $a_u = a_0$, *red* $a_u = 3a_0$, *violet* $a_u = 4a_0$, *blue* $a_u = 6a_0$, *green* $a_u = 8a_0$, *black* $a_u = 16a_0$) of the Type I geometry (cf. Fig. 10)

cross-section only a little, the flow velocities in the utricular region decrease significantly. If we continue to increase the lumen of the utricular region, the flow profile becomes asymmetric with respect of the vertical axis (Fig. 11a) and the peak velocity moves toward the outer wall, while the velocities close to the inner wall decrease. For $a_u/a_0 \geqslant 4$, these velocities change direction, which leads to a vortex. When the dimension of the utricular lumen is increased even further, the velocities on the horizontal axis of the central utricular cross-section increase, and we clearly recognize the S-shape velocity profile typical of a vortex.

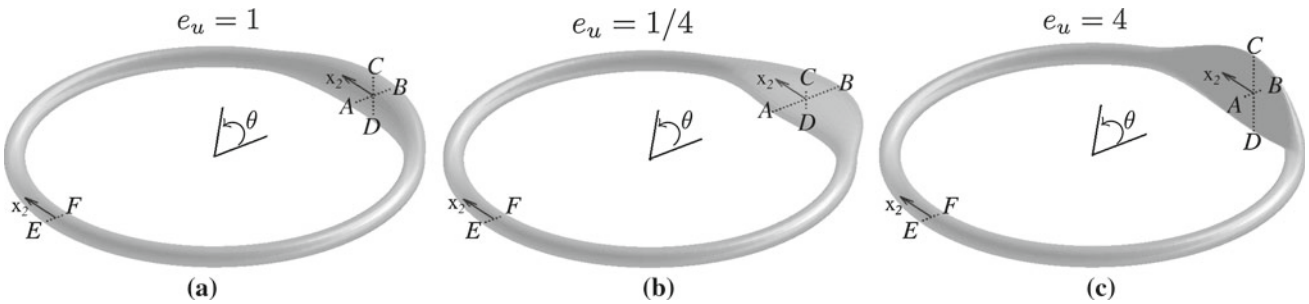

Fig. 12 (**a**) Type I, (**b**) Type II, and (**c**) Type III geometries for a ratio $a_u/a_0 = 4$. $\overline{AB}$ and $\overline{CD}$ are the horizontal and vertical axes of the central utricular cross-section, respectively; $\overline{EF}$ is the diameter of the slender duct; $e_u = \overline{CD}/\overline{AB}$ is the resulting utricular ellipticity; $\overline{AB} = \overline{CD} = 2\overline{EF}$ for the Type I geometry (**a**), $\overline{CD} = \overline{EF}$ for the Type II geometry (**b**), and $\overline{AB} = \overline{EF}$ for the Type III geometry (**c**)

The velocity profile along the vertical axis of the utricular cross-section (Fig. 11b) remains symmetric with respect to the horizontal axis and the velocity magnitude decreases with increasing a_u. Apparently, the observed vortex has a strongly two-dimensional character in the plane of rotation. The flow profiles in the slender duct (Fig. 11c) are well approximated by a parabola. The flow velocities increase slightly with a_u for small ratios a_u/a_0. For bigger (more physiological) ratios a_u/a_0, however, the viscous forces acting on the endolymph within the slender region become dominant and the flow velocities in the slender canal stop increasing. This is consistent with the result of Van Buskirk (1977): the flow in the utricle (here a vortex) does not influence significantly the flow in the canal. A reduction of the angle β spanned by the utricular region leads to similar conclusions, but reduces the velocities of the vortex.

Because the ellipticity of the cross-sections is a well-documented feature of the anatomy of the labyrinth (Curthoys and Oman 1987), we now compare results obtained for the Type I geometry to those of the Type II and Type III geometries (Fig. 12). These geometries have the same cross-sectional areas $a(\theta)$ along the centerline, but a different ellipticity of the utricular region. The obtained flow profiles are compared in Fig. 13 for $\beta = 0.42\pi$ and $a_u/a_0 = 4$. The maximum velocities along the vertical axis of the central utricular cross-section (Fig. 13b) and in the slender region (Fig. 13c) are almost identical for the three geometries. The flow rate is not influenced significantly by the ellipticity of the utricle. However, the ellipticity of the utricle influences significantly the velocity profile along the horizontal axis of the central utricular cross-section (Fig. 13a). The maximum velocity in the utricular region is observed for the Type II geometry ($e < 1$) for which the S-shape profile is most pronounced (strongest vortex). In contrast, we do not observe any vortex for the Type III geometry ($e > 1$), where the velocities in the utricle are smaller and deviate only little from a parabolic profile. The projection of a Type III geometry onto the plane of rotation yields a two-dimensional slender annulus of constant cross-sectional radius.This confirms the two-dimensional nature of

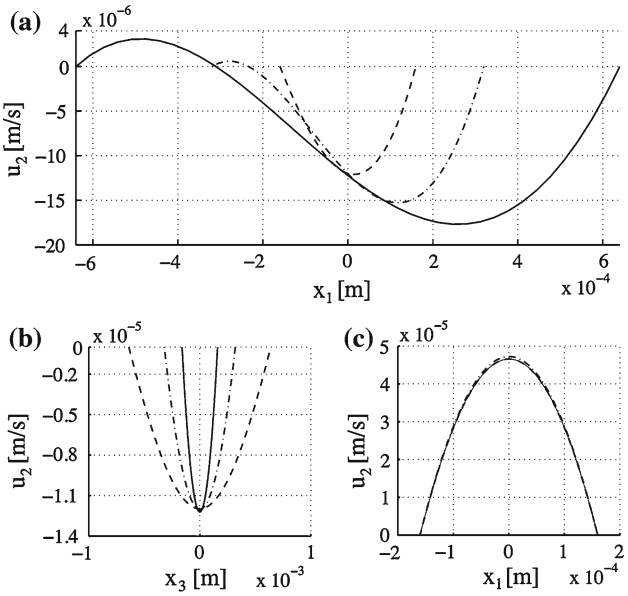

Fig. 13 Axial velocity u_2 evaluated for $\ddot{\alpha} = 120°/s^2$ along the (**a**) horizontal ($\overline{AB}$) and (**b**) vertical ($\overline{CD}$) axes of the cross-section at the center of the utricular region ($\theta = 0$) and (**c**) along the horizontal axis ($\overline{EF}$) of the opposite cross-section in the slender duct (at $\theta = \pi$). The zeros of the abscissae correspond to the center of the cross-section. The results are obtained for the Type I (*dashed line with dot*), Type II (*solid line*), and Type III (*dashed line*) geometries with $a_u/a_0 = 4$ (cf. Fig. 12)

the observed vortex. The flow patterns deviating significantly from a parabolic profile are most favored by a utricular lumen which exceeds the dimension of the slender duct in the plane of rotation. Consistently, results from two-dimensional simulations (Boselli et al. 2009) led to good approximations of the flow velocities in the canal.

An enlargement of the utricle in the plane perpendicular to the SCC can enhance the velocities of the vortex if combined with an enlargement of the utricle in the plane of rotation. The widths of the utricular cross-sections for a Type I geometry with $a_u/a_0 = 16$ (Fig. 10c) and a Type II geometry with $a_u/a_0 = 4$ (Fig. 12b) are very similar, but the vertical extent of the Type I geometry is much bigger, which leads

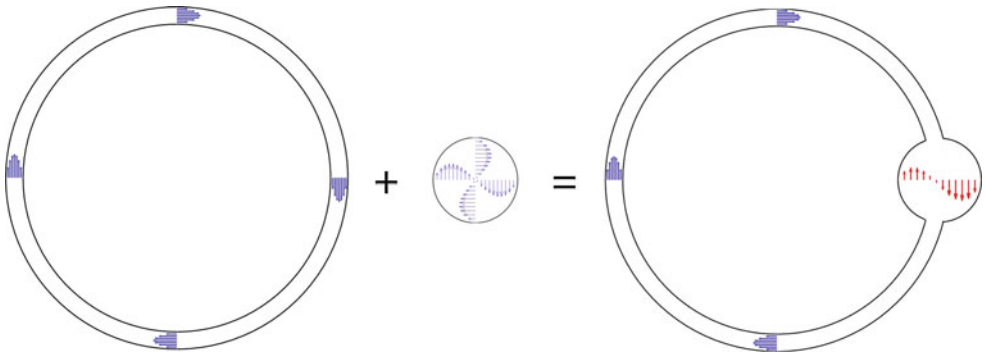

Fig. 14 Velocity vectors (*arrows*) describing the velocity profiles in a two-dimensional annulus (*left*), a disk (*center*), and an idealized one-canal model (*right*). The flow velocities at the cross-section cutting the center of the utricular disk (*red arrows*) are approximated as the superposition of a Poiseuille-like flow and the vortex observed in the disk. If the disk was associated to the ampulla, the crista would be at the right-side of the disk

to a faster vortex (cf. Fig. 11 for $a_u/a_0 = 16$ and Fig. 13 for $a_u/a_0 = 4$).

To show the influence of the cupula stiffness on these results, we repeated some simulations with cupula stiffnesses K corresponding to the range of values of τ_c reported in the literature. It turns out that the influence of the cupula on the flow profiles in the utricular bulge is negligible ($\mathbf{u}_c \ll \mathbf{u}_\alpha$).

By comparing the above results and the available data on the anatomy of the membranous labyrinth, we can be confident about the presence of the vortex in the enlarged part of the labyrinth. The symmetry of the flow profile is broken as soon as the dimension of the bigger chambers in the plane of rotation exceeds the dimension of the narrow duct. We observe a small vortex already for $a_u/a_0 = 4$. The velocities of the vortex increase with a_u/a_0 (in contrast to a Poiseuille flow for which the velocities decrease) and the typical cross-sectional area of the utricle and the ampulla is one order of magnitude bigger than in the slender duct. Therefore, we expect the observed vortex to exist regardless of morphological details not included in our model.

3.3 Heuristic model: an intuitive interpretation of the vortical flow

The results of our simulations become more clear if we consider the two-dimensional flow $\mathbf{u}_s$ in an accelerated disk (Appendix D),

$$\mathbf{u}_s(r) = \frac{\ddot{\alpha}}{8\nu}(-r R_u^2 + r^3)\mathbf{e}_\theta \equiv u_s \mathbf{e}_\theta \tag{10}$$

where $\nu = \mu/\rho$ is the kinematic viscosity of the fluid, r is the distance from the center of the disk, $\mathbf{e}_\theta$ is the unit vector in the azimuthal direction and R_u is the radius of the disk. Equation (10) is an exact solution of the Stokes equations (2) with $\mathbf{f} = \mathbf{f}_\alpha$ and describes a symmetric vortex concentric with the disk. We connect this disk to an annulus of cross-sectional radius $a_{\mathrm{scc}} = 0.16$ mm and major radius $R_{\mathrm{scc}} = 3$ mm

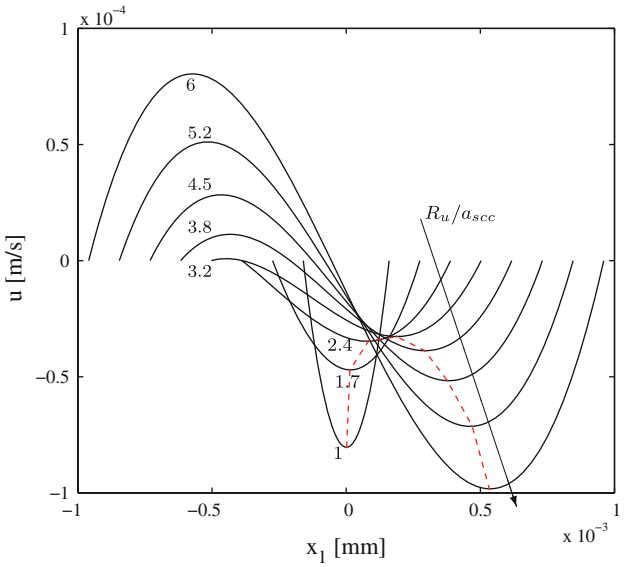

Fig. 15 Flow velocity u (*solid lines*) predicted by the heuristic model for different ratios of the utricular and SCC cross-sectional radii ($R_u/a_{\mathrm{scc}} = 1, 1.71, 2.42, \ldots, 6$; $a_{\mathrm{scc}} = 0.16$ mm; $\ddot{\alpha} = 120°/\mathrm{s}^2$). The *dashed line* shows the position and the magnitude of the peak velocity obtained increasing R_u/a_{scc}. The results for this heuristic model should be compared to the numerical results in Fig. 11

(Fig. 14). The disk and the annulus represent an idealized utricle and SCC, respectively. The flow in the utricular disk can then be approximated as the superposition of the vortical flow (10) and a Poiseuille-like flow whose flow rate is equal to the flow rate in the accelerated annulus (Appendix D). This flow provides a heuristic model of the vortical flow observed in our transient simulations.

Figure 15 shows the evolution of the flow profile in the utricular disk of the idealized SCC in Fig. 14. The ratio R_u/a_{scc} is increased from 1 to 6. Initially, the velocities decrease. But for $R_u/a_{\mathrm{scc}} \gtrsim 3$, we observe the formation of a vortex and the velocities increase with the dimension of the

utricular disk. These qualitative results are consistent with the numerical results reported in Fig. 11a for three-dimensional geometries. For the sake of clarity, we point out that the heuristic model is a substantial simplification of the labyrinth. Its goal is to provide a basic explanation for the formation of the vortical flow. It should not be used to explain the full biology of angular motion transduction which requires the introduction of a cupula and other important anatomical features. To this end, one should instead refer to the numerical model.

4 Discussion

The proposed numerical model for the endolymph flow allows us to access not only the averaged quantities predicted by analytical models, but also the local flow velocities in the proximity of the sensory tissues.

We have limited our investigation to transient, low frequencies head maneuvers and shown a vortical S-shape flow profile in the utricle and the ampulla. On the one hand, this vortex does not significantly influence the macro-mechanics of the SCC and the resulting flow rate leads to a cupula volume displacement consistent with previous investigations and experimental evidences. On the other hand, the observed vortex represents a fundamentally new feature of the endolymphatic flow: It leads to flow velocities in the utricle/ampulla that can be higher than in the slender duct, and it enhances the shear stresses at the utricular macula and at the cristae ampullaris. These numerical results cannot be accessed by state-of-the-art experiments, which are typically based on indirect measurements, for example, the firing rate of vestibular afferents. In this sense, our numerical predictions—based on established, physical principles and computational approaches—are a complement to such experiments.

The presented results are robust with respect to the approximations made for the governing equations as well as for the geometry of the labyrinth. Our simulations have been validated by results computed independently by a finite volume solver for the full Navier-Stokes equations (OpenFOAM). The influence of the anatomy of the labyrinth on our results has been studied in Sect. 3.2: The formation of the vortex is induced by the macroscopic anatomical feature that the enlarged lumen of the labyrinth exceeds the dimension of the slender duct significantly. In humans, typical cross-sectional area ratios a_u/a_0 are approximately up to twenty-five in the utricle and up to thirteen in the ampulla. For these values and based on the data shown in Fig. 11, we have to expect a vortex independently of other morphological details.

In the remainder of the paper, we speculate on the clinical and physiological implications of the observed vortex.

4.1 Physiological and clinical implications of the vortex in the utricle

It is well known that mechanical signals are as important as chemical ones during the growth of many living tissues (e.g. Cowin 2004). We have shown in Sect. 3.1.1 that the ellipticity of the utricular cross-sections leads to peak shear stresses at the position of the macula for rotations in any direction. These are one order of magnitude higher than the values predicted for a parabolic flow profile. It would come as no surprise if the local distribution of the hair cells was related to the vortex.

The vortical flow, for example, could help to explain the lack of otolith contribution to the vestibular ocular reflex during off-vertical axis yaw head rotations reported by Bockisch et al. (2005). For yaw rotations, the directions of the shear stresses at the macula are not uniform because the vortex rotates in the plane of the macula for angular accelerations in the plane of the HC (Fig. 7). Possible afferent signals from the different regions of the macula might then cancel each other. The sensitivity threshold $\tau_{\min}$ for the shear stress on the macula can be approximated from the magnitude of the force per unit area induced by the smallest linear acceleration $a_{\min} \approx 2 \times 10^{-3}\ g$ that can be sensed by the macula, where g is the gravitational acceleration (Peters 1969). A rough approximation of $\tau_{\min}$ based on the values reported in Rabbitt et al. (2004) is

$$\tau_{\min} \approx a_{\min}(\rho_o - \rho_f)b \approx 2 \times 10^{-4}\ \text{Pa}$$

where $b \approx 30\ \mu\text{m}$ is the thickness of the otoconial layer and ρ_o and ρ_f are the otoconial layer and endolymph densities. For an angular acceleration of $120°/s^2$, we obtain wall shear stresses at the macular region of up to approximately 7×10^{-4} Pa (Fig. 7). This value is slightly above the sensitivity threshold $\tau_{\min}$. However, this is not sufficient to ground a functional role of the vortical flows because this result suggests that the contribution of the fluid to the otolith mechanics is very small compared to the contribution of typical gravitational/inertial forces. It will be necessary to couple the detailed fluid dynamics in the utricle to realistic models of the otolith organ (e.g. Jaeger et al. (2002), which takes the directionality of the hair cells into account) in order to better understand a possible functional role of the vortex in the macula response.

A vortical flow favors the response of the papilla neglecta

More intuitively than for the macula, a vortical flow would favor the response of the papilla neglecta (PN), if present. In many vertebrates, the PN occupies a small region of the utricular wall in addition to the macula. It consists of a few hair cells embedded in a short cupula ($\approx 60\ \mu m$), which protrudes into the utricular lumen. Brichta and Goldberg (1998)

showed that the PN of the turtle responds to angular accelerations and angular jerk. No otoconia are present on the PN such that the forces leading to the mechanotransduction come only from the endolymph velocity—which are enhanced by the observed vortex. A PN has been observed also in some human posterior ampullae, but its functionality is still under debate (Brichta and Goldberg 1998).

The endolymph velocity increases under conditions of endolymphatic hydrops

The parametric study Sect. 3.2 shows that an increase in the dimension of the utricular region, for example, because of a pressure increase of the endolymphatic compartment (hydrops), will lead to an increase in the velocities in the utricle. In contrast, the velocities would be reduced if there was a Poiseuille-like flow.

4.2 A vortical flow may favor the mechanotransduction in the ampulla

We now discuss some advantages in having a vortical flow, rather than a Poiseuille flow, in the ampulla. To this end, we define the SCC gain in terms of angular cupular displacement at the crista (like in Damiano and Rabbitt 1996). This quantity is intrinsically related to the transverse shear strain of the hair bundles, which is the major mechanism responsible for hair cell activation.

Our results suggest that a vortical flow may increase the SCC gain: The asymmetric flow profile of the vortical flow favors the displacement of the cupula closer to the crista rather than at the center of the cupula. Moreover, the ellipticity of the cupular cross-sections is such that the distribution of the shear stresses at the wall of the ampulla shows maximum values at the outer equatorial region of the ampulla where the crista is located.

Dohlman (1980) observed that animals with high sensitivity to vestibular stimuli have a cupular cross-sectional area significantly bigger (e.g. 36 times for the owl) than the cross-section of the slender duct. A bigger cupula helps to transduce head rotations at very low frequencies by increasing τ_c ($\tau_c \propto 1/K$ and K decreases with the diameter of the cupula). For a Poiseuille flow, a bigger cupula can also reduce the SCC gain because of a reduced average cupula displacement (e.g. Squires 2004). In contrast, a vortical flow has the potential to preserve, or even increase the gain of the SCC for a bigger ampulla: In our simulations, angular acceleration leads to velocity magnitudes in the proximity of the crista similar to the velocities in the slender duct, even if the displacement of the endolymph averaged over the cross-section is much smaller. Moreover, increasing the cross-section of the cupula increases the velocities in the proximity of the crista.

We also point out that an S-shape velocity profile allows local deflections of the cupula even for a zero average-displacement of the cupula. This favors the transduction in a SCC even after complete surgical occlusion of the lumen, for which the macro-mechanics of the SCC relies on the elasticity of the membranous wall (Rabbitt et al. 1999, 2006).

At this point, we are only able to give qualitative results on the deflected shape of the cupula. More conclusive results will require a full coupling of the detailed fluid dynamics in the ampulla with a more detailed model of the cupula (e.g. Selva et al. 2009).

No vortex in positional flows

The observed vortex is induced by angular acceleration and is not expected in "positional flows", for example, during benign paroxysmal positional vertigo symptoms in canalithiasis (Rajguru et al. 2004; Obrist and Hegemann 2008; Boselli et al. 2010a) or mechanical indentation (Dickman and Correia 1989). We point out that this observation is not in contradiction with results on the mechanical indentation reported by Rabbitt et al. (1995) for the toadfish. They could model successfully the relationship between rotation and indentation by matching the average cross-sectional pressure for the two different stimuli. Results from our parametric study (cf. Figs. 11a, b; $4 \lesssim a_u/a_0 \lesssim 10$ in the toadfish) suggests that including the vortical flow in their macro-mechanical model would increase the cupula displacement and the angular displacement at the crista up to a factor of five and ten, respectively. A shift of the predictions in Rabbitt et al. (1995) by a factor below ten would still lead to a good match between predictions and measurements because of the significant inter-afferent variability in the measured rotation-to-indentation gain.

5 Concluding remarks

Our numerical computations predict a vortical flow in the utricle and the ampulla when there is angular acceleration (or deceleration). As a consequence, the common assumption of axisymmetric flow profiles in the utricle and the ampulla leads to a loss of essential information on the flow in the proximity of the sensory epithelia. The predicted vortex depends on typical macroscopic anatomical features of the labyrinth. For the model used in our parametric study, the vortex is observed when the dimension of the utricol/ampulla bulge in the plane of rotation is at least two times bigger than the diameter of the narrow part of the SCC (cf. Fig. 13). The vortical flow maximizes the shear stresses at the sensory epithelia and suggests a non-axisymmetric deflection of the cupula. The presented results may serve to shed light on

open physiological issues and be useful guidelines for future studies on the mechanics of the vestibular system.

Acknowledgments The work of F.B. was supported by the Swiss National Science Foundation (SNF # 200021-116575).

Appendices

Appendix A: Flow $\mathbf{u}_c$ due to the cupula

We approximate the cross-sections of the endolymph duct by ellipses. Following the approach of Oman et al. (1987), we have

$$\mathbf{u}_c(y,z,\theta,t) \approx 8KV(t)/H(a_1a_2\pi)^{-1}\left[1-\left(\frac{z^2}{a_2^2}+\frac{y^2}{a_1^2}\right)\right]\mathbf{n} \quad (11)$$

where the local coordinates $z(\theta)$ and $y(\theta)$ are taken along the semiaxes $a_1(\theta)$ and $a_2(\theta)$, respectively, $\mathbf{n}(\theta)$ is the unit vector normal to the surface of the cross-section, and θ is the azimuthal position of the cross-section with respect to the center of mass of the fluid domain. H is the hydraulic resistance of the complete endolymphatic duct,

$$H \equiv \int_{-\pi}^{\pi} \frac{\pi a_1^3 a_2^3}{4\mu(a_1^2+a_2^2)}\mathrm{d}\theta. \quad (12)$$

Appendix B: Derivation of $\mathbf{f}_\alpha$

The most general expression for the fictitious force $\mathbf{f}_\alpha$ due to inertia is (Kundu and Cohen 2002)

$$\mathbf{f}_\alpha(\mathbf{x},t) = \rho\mathbf{a}_c + \rho\ddot{\boldsymbol{\alpha}}\times\mathbf{x} + \rho\dot{\boldsymbol{\alpha}}\times(\dot{\boldsymbol{\alpha}}\times\mathbf{x}) + 2\rho\dot{\boldsymbol{\alpha}}\times\mathbf{u} \quad (13)$$

where $\mathbf{a}_c$ is the linear acceleration, $\ddot{\boldsymbol{\alpha}}$ the angular acceleration and $\dot{\boldsymbol{\alpha}}$ the angular velocity of the system, all measured in an inertial reference frame. Without loss of generality, the center of rotation is set at the origin. From left to right, the terms in Eq. (13) represent: the inertial force arising from $\mathbf{a}_c$, the force due to $\ddot{\boldsymbol{\alpha}}$, and the centrifugal and the Coriolis forces due to $\dot{\boldsymbol{\alpha}}$. The linear acceleration and the centrifugal terms can be rewritten as the gradient of a scalar potential function and eliminated from the right-hand side of Eq. (13) by replacing p with the modified pressure

$$p^* = p - \rho[\mathbf{a}_c + \dot{\boldsymbol{\alpha}}\times(\dot{\boldsymbol{\alpha}}\times\mathbf{x})]\cdot\mathbf{x}. \quad (14)$$

Neglecting the Coriolis term, Eq. (13) is reduced to (6) which depends only on the angular acceleration of the system. The Coriolis term turns out to be negligible for the discussed head maneuver (low velocities and low frequencies). This approximation has also been validated by simulations including the complete force (13) and computed by a finite volume solver for the full Navier-Stokes equations (OpenFOAM).

Appendix C: Numerical solution of the endolymph flow

The velocity field $\mathbf{u}_\alpha$ is evaluated as the superposition of a particular $\mathbf{u}_p$ and a homogeneous $\mathbf{u}_h$ solution,

$$\mathbf{u}_\alpha = \mathbf{u}_p + \mathbf{u}_h. \quad (15)$$

The particular solution $\mathbf{u}_p$ of (2) for $\mathbf{f}_\alpha(\mathbf{x},t) = \rho\ddot{\boldsymbol{\alpha}}\times\mathbf{x}$ is

$$\mathbf{u}_p = \frac{\ddot{\alpha}}{8\nu}r^3\mathbf{e}_\theta. \quad (16)$$

It was derived by replacing $\mathbf{u}$ in the azimuthal component of the momentum equation with the ansatz

$$\mathbf{u}_p = u_p\mathbf{e}_\theta = \gamma r^3\mathbf{e}_\theta, \quad (17)$$

where γ is a constant, r is the radial coordinate, and $\mathbf{e}_\theta$ is the unit vector in the azimuthal direction.

C.1 Homogeneous solution

The homogeneous solution $\mathbf{u}_h$ has to satisfy Eq. (2) with $\mathbf{f}=0$ and the boundary conditions

$$\mathbf{u}_h|_{\partial\Omega} = -\mathbf{u}_p|_{\partial\Omega} \quad (18)$$

where $\partial\Omega$ is the boundary of the fluid domain Ω. This enforces the no-slip boundary conditions $\mathbf{u}_\alpha|_{\partial\Omega}=0$. The homogeneous solution $\mathbf{u}_h$ cannot be derived analytically for a general domain Ω. We solve it numerically by the MFS (Golberg and Chen 1999; Young et al. 2006). The fundamental solution of the Stokes equations is the *Stokeslet* (Pozrikidis 1992; Chwang and Wu 1975). A Stokeslet satisfies the equations everywhere except at its singularity (source point). We find $\mathbf{u}_h$ as the superposition of N Stokeslets with their singularities positioned outside the flow domain Ω,

$$\mathbf{u}_h(\mathbf{x}) = \sum_{k=1}^{N}\mathbf{S}(\hat{\mathbf{x}})\mathbf{w}_k \quad (19)$$

where $\mathbf{x}$ are the Cartesian coordinates, $\hat{\mathbf{x}} = \mathbf{x}-\mathbf{y}_k$ and $\mathbf{y}_k$ is the coordinate of the singularity of the kth Stokeslet; the 3×1 vectors $\mathbf{w}_k$ are the strengths of the Stokeslets and $\mathbf{S}$ is the Stokeslet tensor,

$$S_{ij}(\hat{\mathbf{x}}) = \frac{1}{8\pi\mu}\left[\frac{1}{r}\delta_{ij}+\frac{\hat{x}_i\hat{x}_j}{r^3}\right] \quad (20)$$

with $r=|\hat{\mathbf{x}}|$. The parameters $\mathbf{w}_k$ are determined by enforcing the boundary conditions at M collocation points on the boundary $\partial\Omega$. This leads to a linear system of equations, which we solve in the sense of least squares. The source points $\mathbf{y}_k$ are positioned on multiple layers embracing the surface $\partial\Omega$ with the help of the block greedy-QR algorithm

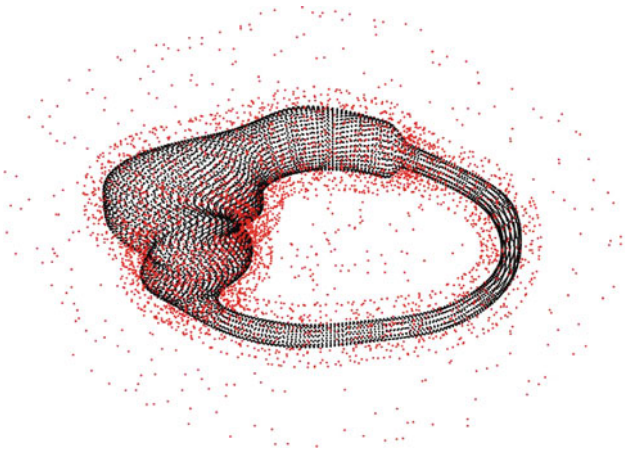

Fig. 16 Collocation points (*black dots*) and source points (*red dots*) used for the flow computation for the geometry introduced in Sect. 3.1 (cf. Fig. 3)

described by Boselli et al. (2010b). Figure 16 shows the position of the collocation and source points used to approximate $\mathbf{u}_h$ on the fluid domain introduced in Sect. 3.1.

Appendix D: Exact solutions for a two-dimensional annulus and a disk

The exact solution $\mathbf{u}_{\rm scc} = u_{\rm scc}\mathbf{e}_\theta$ of (2) with $\mathbf{f} = \mathbf{f}_\alpha$, for the two-dimensional annulus in Fig. 14, is

$$\mathbf{u}_{\rm scc} = \frac{\ddot{\alpha}}{8\nu}\left[r^3 - 2r(R_{\rm scc}^2 + a_{\rm scc}^2)\right]\mathbf{e}_\theta + \frac{\ddot{\alpha}}{8\nu}\left[\frac{(R_{\rm scc}+a_{\rm scc})^2(R_{\rm scc}-a_{\rm scc})^2)}{r}\right]\mathbf{e}_\theta, \qquad (21)$$

where r is the radial coordinate. This was derived analytically as a superposition of the particular solution (16), a two-dimensional *roton* and a two-dimensional *rotlet* (Pozrikidis 1992; Chwang and Wu 1975). For physiological values of $a_{\rm scc}$, (21) is well approximated by a parabola.

The exact flow field (10) for the disk of Fig. 14 was derived as the superposition of the particular solution (16) and a roton.

References

Abramowitz M, Stegun IA (eds) (1992) Handbook of mathematical functions with formulas, graphs, and mathematical tables, reprint of the 1972 edn. Dover Publications, Inc., New York

Bernard C (1982) Theoretical aspects of cupula deflection in semicircular canals. J Theor Biol 98:637–643

Bockisch CJ, Straumann D, Haslwanter T (2005) Human 3-d aVOR with and without otolith stimulation. Exp Brain Res 161: 358–367. doi:10.1007/s0022100420801

Boselli F, Obrist D, Kleiser L (2009) Numerical simulation of the flow in semicircular canals with the method of fundamental solutions. Proc Appl Math Mech 9(1): 485–486. doi:10.1002/pamm.200910215

Boselli F, Obrist D, Kleiser L (2010a) A meshless boundary method for computation of Stokes flow with particles in the semicircular canals of the inner ear. Proc Appl Math Mech 10(1): 1617–7061. doi:10.1002/pamm.201010222

Boselli F, Obrist D, Kleiser L (2010b) Multilayer MFS for Stokes problems. In: Sarler B, Atluri SN (eds) Recent studies in meshless and other novel computational methods. Tech Science Press, Encino pp 71–86

Brichta AM, Goldberg JM (1998) The papilla neglecta of turtles: a detector of head rotations with unique sensory coding properties. J Neurosci 18(11):4314–4324

Chwang AT, Wu TYT (1975) Hydromechanics of low-Reynolds-number flow. Part 2 Singularity method for Stokes flows. J Fluid Mech 67(04):787–815

Cowin SC (2004) Tissue growth and remodeling. Annu Rev Biomed Eng 6: 77–107. doi:10.1146/annurev.bioeng.6.040803.140250

Curthoys IS, Oman CM (1987) Dimensions of the horizontal semicircular duct, ampulla and utricle in the human. Acta Otolaryngol 103:254–261

Curthoys IS, Markham CH, Curthoys EJ (1977) Semicircular duct and ampulla dimensions in cat, guinea pig and man. J Morph 151: 17–34. doi:10.1002/jmor.1051510103

Damiano ER, Rabbitt RD (1996) A singular perturbation model of fluid dynamics in the vestibular semicircular canal and ampulla. J Fluid Mech 307(1): 333–372. doi:10.1017/S0022112096000146

Dickman JD, Correia MJ (1989) Responses of pigeon horizontal semicircular canal afferent fibers. I. Step, trapezoid, and low-frequency sinusoid mechanical and rotational stimulation. J Neurophysiol 62:1090–1101

Dohlman G (1980) Critical review of the concept of cupula function. Acta Oto-Laryngol 90(S376):2–30

Golberg MA, Chen CS (1999) The method of fundamental solutions for potential, Helmholtz and diffusion problems. In: Golberg M (ed) Boundary integral methods: numerical and mathematical aspects. WIT Press/Computational Mechanics Publications, Boston/Southampton pp 105– 176

Grant JW (1995) Vestibular mechanics. In: Bronzino JD (ed) Biomedical engineering handbook, chap 64. CRC Press, Boca Raton, Florida, pp 1–16

Grant JW, Van Buskirk WC (1976) Experimental measurement of the stiffness of the cupula. Biophys J 16(6): 669–678. doi:10.1016/S0006-3495(76)85720-7

Ifediba MA, Rajguru SM, Hullar TE, Rabbitt RD (2007) The role of 3-canal biomechanics in angular motion transduction by the human vestibular labyrinth. Ann Biomed Eng 35(7): 1247–1263. doi:10.1007/s10439-007-9277-y

Jaeger R, Takagi A, Haslwanter T (2002) Modeling the relation between head orientations and otolith responses in humans. Hear Res 173(1–2): 29–42. doi:10.1016/S0378-5955(02)00485-9

Kachar B, Parakkal M, Fex J (1990) Structural basis for mechanical transduction in the frog vestibular sensory apparatus: I. The otolithic membrane. Hear Res 45(3): 179–190. doi:10.1016/0378-5955(90)90119-A

Kondrachuk A, Shipov A, Astakhova T, Boyle R (2011) Current trends in mathematical simulation of the function of semicircular canals. Hum Physiol 37:802–809. doi:10.1134/S0362119711070164

Kundu PK, Cohen IM (2002) Fluid mechanics. Academic Press, London

Obrist D (2008) Fluidmechanics of semicircular canals—revisited. Z Angew Math Phys 59: 475–497. doi:10.1007/s00033-007-6037-7

Obrist D, Hegemann S (2008) Fluid–particle dynamics in canalithiasis. J R Soc Interface 5(27): 1215–1229. doi:10.1098/rsif.2008.0047

Obrist D, Hegemann S, Kronenberg D, Häuselmann O, Rösgen T (2010) In vitro model of a semicircular canal: design and

validation of the model and its use for the study of canalithiasis. J Biomech 43(6): 1208–1214. doi:10.1016/j.jbiomech.2009.11.027

Oman CM, Marcus EN, Curthoys IS (1987) The influence of semicircular canal morphology on endolymph flow dynamics. An anatomically descriptive mathematical model. Acta Otolaryngol 103(1): 1–13. doi:10.3109/00016488709134691

Pardoe K, Haughton PM (1979) The flow of endolymph in the semicircular canals. J Neurosci 24(5):1009–1013

Peters R (1969) Dynamics of the vestibular system and their relation to motion perception, spatial disorientation, and illusions. CR-1309, NASA

Pozrikidis C (1992) Boundary integral and singularity methods for linearized viscous flow. Cambridge texts in applied mathematics. Cambridge University Press, Cambridge

Rabbitt RD, Damiano ER (1992) A hydroelastic model of macromechanics in the endolymphatic vestibular canal. J Fluid Mech 238(1): 337–369. doi:10.1017/S0022112092001745

Rabbitt RD, Boyle R, Highstein SM (1995) Mechanical indentation of the vestibular labyrinth and its relationship to head rotation in the toadfish, opsanus tau. J Neurophysiol 73(6):2237–2260

Rabbitt RD, Boyle R, Highstein SM (1999) Influence of surgical plugging on horizontal semicircular canal mechanics and afferent response dynamics. J Neurophysiol 82(2):1033–1053

Rabbitt RD, Damiano ER, Grant JW (2004) Biomechanics of the semicircular canals and otolith organs. In: Highstein SM, Fay R, Popper AN (eds) The vestibular system, Springer handbook of auditory research, vol 19. Springer, New York pp 153–201. doi:10.1007/0-387-21567-0_4

Rabbitt RD, Boyle R, Highstein SM (2006) Physiology of the semicircular canals after surgical plugging. Ann NY Acad Sci 942:274–286

Rabbitt RD, Breneman KD, King C, Yamauchi AM, Boyle R, Highstein SM (2009) Dynamic displacement of normal and detached semicircular canal cupula. JARO-J Assoc Res Oto 10: 497–509. doi:10.1007/s10162-009-0174-y

Rajguru SM, Ifediba MA, Rabbitt RD (2004) Three-dimensional biomechanical model of benign paroxysmal positional vertigo. Ann Biomed Eng 32: 831–846. doi:10.1023/B:ABME.0000030259.41143.30

Selva P, Oman CM, Stone HA (2009) Mechanical properties and motion of the cupula of the human semicircular canal. J Vestibul Res-Equil 19(3): 95–110. doi:10.3233/VES-2009-0359

Squires TM (2004) Optimizing the vertebrate vestibular semicircular canal: could we balance any better? Phys Rev Lett 93:198,106. doi:10.1103/PhysRevLett.93.198106

Steer RW, Li YT, Young LR, Meiry JL (1967) Physical properties of the labyrinthine fluids and quantification of the phenomenon of caloric stimulation. Third symposium on the role of the vestibular organs in space exploration NASA SP-152, pp 409–512

Van Buskirk WC (1977) The effect of the utricle on fluid flow in the semicircular canals. Ann Biom Eng 5:1–11. doi:10.1007/BF02409335

Van Buskirk WC, Watts RG, Liu YK (1976) The fluid mechanics of the semicircular canals. J Fluid Mech 78(01): 87–98. doi:10.1017/S0022112076002346

Vega R, Alexandrov VV, Alexandrova TB, Soto E (2008) Mathematical model of the cupula-endolymph system with morphological parameters for the Axolotl (*Ambystoma tigrinum*) semicircular canals. Open Med Inform J 2:138–148

Yamauchi A, Rabbitt RD, Boyle R, Highstein SM (2002) Relationship between inner-ear fluid pressure and semicircular canal afferent nerve discharge. JARO-J Assoc Res Oto 3: 26–44. doi:10.1007/s101620010088

Young DL, Jane SJ, Fan CM, Murugesan K, Tsai CC (2006) The method of fundamental solutions for 2D and 3D Stokes problems. J Comput Phys 211(1): 1–8. doi:10.1016/j.jcp.2005.05.016